Arabian Journal of Geosciences (2019) 12: 497
https://doi.org/10.1007/s12517-019-4598-3

ORIGINAL PAPER

Geology, geochronology, and fluid evolution of the Pingshun skarn iron deposit, southern Taihang Mountains

Haidong Zhang [1,2] · Dequan Wang [3] · Jianchao Liu [1] · Jinkun Yang [1]

Received: 6 July 2018 / Accepted: 28 June 2019 / Published online: 5 August 2019

Abstract

The Pingshun skarn iron deposit is located in the southern Handan–Xingtai iron district of the southern Taihang Mountains, North China Craton. Skarns and ore bodies occur as lamina, lenses, and veins along the contact between a dioritic pluton and carbonates of the Middle Ordovician Majiagou Formation. The paragenetic sequence is albite followed by diopside, then garnet, magnetite, and finally calcite. Diorite and olivine-bearing hornblende gabbro in the Pingshun area contain zircon grains with SHRIMP U–Pb ages of 123.4 ± 1.7 and 125.5 ± 2.3 Ma, respectively. Based on the close spatial association between diorite and mineralization, we suggest that both magma activities and iron mineralization in the Pingshun area took place at 125–123 Ma. Three types of fluid inclusions identified in minerals from the Pingshun deposit include three-phase (type 1), two-phase (type 2), and pure liquid (type 3) inclusions. The ore-forming fluid evolved from high temperature (515–679 °C) with high salinity (39.8–77.6 wt% NaCl equiv.) in diopside, to medium–high temperature (365–496 °C) with moderate–low salinity (11.8–17.6 wt% NaCl equiv.) in garnet, and to low temperature (162–295 °C) with moderate–low salinity (6.7–35.5 wt% NaCl equiv.) in calcite. The presence of hematite, halite, and gypsum daughter minerals in type 1 fluid inclusions and the occurrence of andradite in skarns indicate that the pre-ore–forming fluid was oxidized. The $\delta^{34}S$ values of pyrite separated from ores vary from 12.5 to 17.4‰, with $^{206}Pb/^{204}Pb = 17.26–19.03$, $^{207}Pb/^{204}Pb = 15.42–15.69$, and $^{208}Pb/^{204}Pb = 37.29–39.76$, suggesting the ore-forming fluid was originated from a magmatic source and with additional crustal material during the mineralization process. This is consistent with H–O isotope data ($\delta^{18}O_{diopside\text{-}H2O} = 10.8‰$, $\delta^{18}O_{garnet\text{-}H2O} = 9.5–10.8‰$, $\delta^{18}O_{magnetite\text{-}H2O} = 9.8–13.4‰$, δD_{garnet} varying from − 106 to − 86‰, $\delta D_{diopside} = -90‰$). The microthermometry of fluid inclusions and isotope data reveal that the addition of gypsolyte and salt-bearing marlstone into the ore-forming fluid increases Na, Ca, and Cl and that it significantly increases the ability to transport Fe and enhances the capacity of Fe in the ore-forming fluid. Fluid boiling and additional meteoric water involved are two major key factors controlling the ore precipitation. Mantle materials involved in magma and high oxygen fugacity are considered to be crucial roles in the formation of numerous iron deposits in the Handan–Xingtai iron district.

Keywords Skarn iron deposit · Fluid inclusions · S–Pb–H–O isotope · Microthermometry · Geochronology · Handan–Xingtai iron district

Introduction

Skarn deposits are widely distributed around the world and often contain significant resources of Fe, W, Cu, Pb, Zn, Mo, Ag, Au, U, and rare earth elements (Meinert et al. 2005). In China, skarn iron deposits are the principal sources of high-grade iron ores (Wilde et al. 2002; Zhao et al. 2001; Jin et al. 2015). Several well-known large skarn iron ore districts in North China include the Handan-Xingtai area in Hebei Province (Zheng et al. 2007a, b; Zhang et al. 2013; Shen et al. 2013a), Luxi area in Shandong Province (Zhao et al. 1990; Zong et al. 2010), Anyang area in Henan Province (Chen et al. 2014) and Linfen area in Shanxi Province (Zhang et al. 2010). The Handan–Xingtai iron district, located in the southern Taihang Mountains (Fig. 1a, b), contains numerous skarn iron deposits (such as the Xishimen, Beiminghe iron deposits, with a total reserve of over 1000 Mt) related to Early Cretaceous mafic-intermediate magmatic events.

Editorial handling: Zakaria Hamimi

✉ Haidong Zhang
zhdong@chd.edu.cn

[1] The School of Earth Science and Resources, Chang'an University, Xi'an 710064, China

[2] Department of Geology, Northwest University, Xi'an 710069, China

[3] Sino Shaanxi Nuclear Industry Group, Xi'an, China

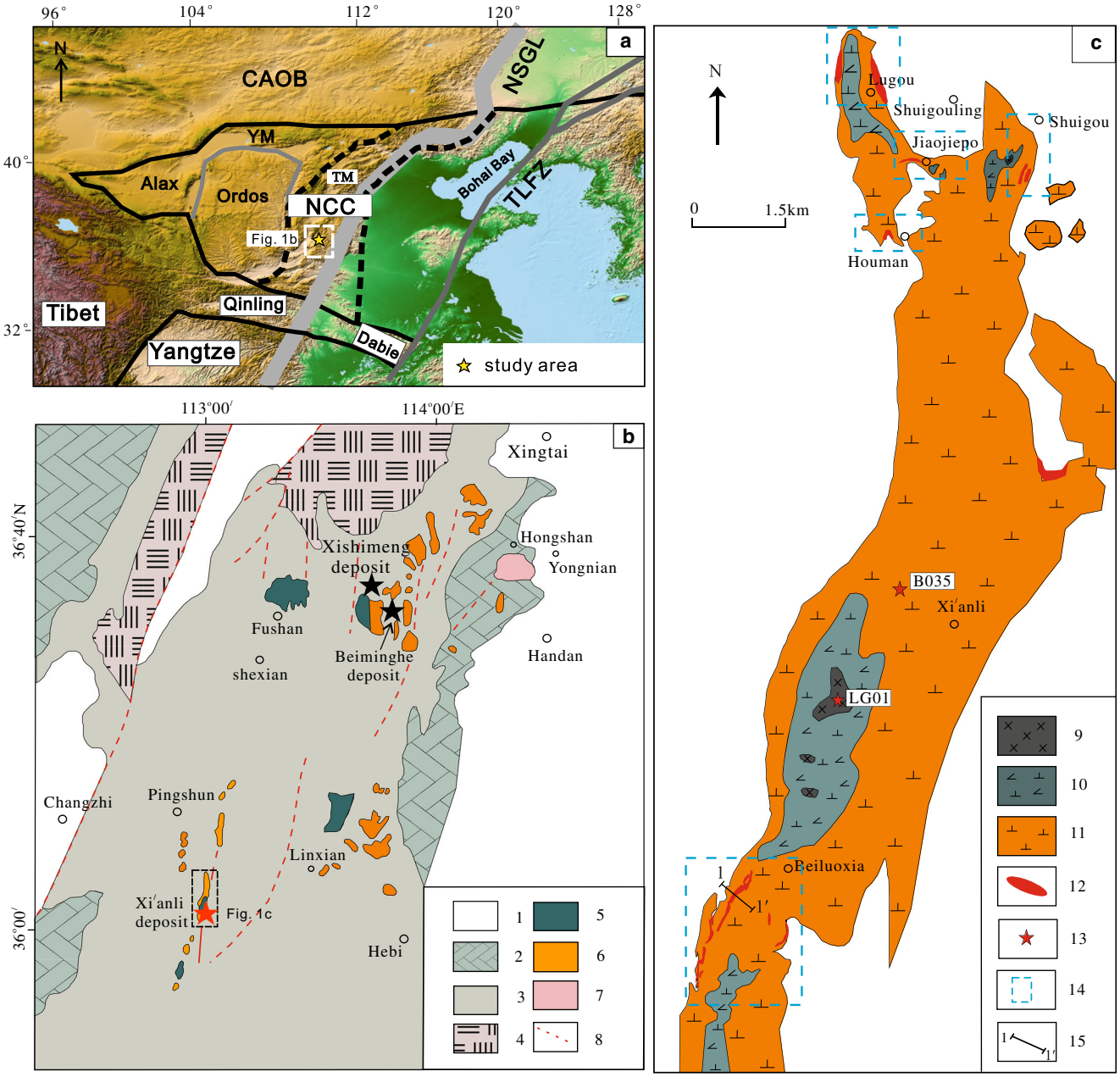

Fig. 1 **a** Location map of the study area and its relationship with the North China Craton. **b** Magmatism and major deposit locations of the Handan–Xingtai iron district (modified from Zhang et al. 2014; Chen et al. 2008; Xu et al. 2010c). **c** Geological map of the Pingshun deposit. 1: Quaternary; 2: Carboniferous–Permian sediment; 3: Middle Ordovician Majiagou Formation; 4: Archaean metamorphic complex; 5: hornblende gabbro; 6: hornblende–diorite; 7: syenite; 8: fault; 9: olivine-bearing hornblende gabbro; 10: hornblende–diorite; 11: diorite–monzodiorite; 12: ore bodies; 13: location of sample; 14: ore block; 15: geological cross-section

Previous studies in the Handan–Xingtai iron district have mostly dealt with geochemistry of ore-related intrusions (Zhang et al. 2014; Xu et al. 2009; Sun et al. 2014; Chen et al. 2004; Shen et al. 1977). However, there some fundamental issues still exist. For example, how to the ore-forming fluid evolved and why the skarn mineralization occured in the Southern Taihang Mountains.

The Pingshun skarn iron deposit is located in the southern part of the Handan–Xingtai iron district of southern Taihang Mountains, 50 km northwest of Pingshun country, Shanxi Province (Fig. 1b). Compared with other skarn iron deposits in the Handan–Xingtai iron district, the Pingshun deposit has well-exposed surface outcrops of typical iron ore bodies and skarn alteration, which provides easy access to conduct petrological studies on iron ore bodies and skarns and to reconstruct the process and spatial distribution of mineralization.

In this paper, we present new data from field and laboratory investigations, including zircon U–Pb age of magma

intrusions, fluid inclusion microthermometry, H–O isotopic data for ore-forming fluids, and S–Pb isotopic data for pyrite for ore-forming materials sources in the Pingshun deposit. These data will provide direct evidence to (1) determine the age of mineralization, (2) reveal the sources of Fe and evolution of ore-forming fluids, and (3) provide more information to reconstruct the process of Fe mineralization.

Regional geology

The Pingshun deposit is located in the southern part of Taihang Mountain and southwestern edge of Handan–Xingtai iron district near the center North China Craton (NCC, Fig. 1a). The Handan–Xingtai iron district extends 200 km long and 40 km wide with NNE-trending. Numerous occurrences of iron deposits with high Fe grade indicate that the Handan–Xingtai iron district is an important iron-rich ore zone with great economic potential in China (Zheng et al. 2006, 2007a). Many iron deposits within the Handan–Xingtai iron district were hosted dominantly by Middle Ordovician carbonates or magmatic bodies (Zheng et al. 2006, 2007a; Zhang et al. 2013).

The major lithological units in the Handan–Xingtai iron district are dominated by a cover sequence of Phanerozoic sedimentary sequences. The Precambrian basement is dominated by the Archean Zanhuang Groups which are mainly composed of tonalite–trondhjemite–granodiorite (TTG) gneisses, marble, and amphibolites (Li et al. 2013; Zhai and Santosh 2011). The Phanerozoic sedimentary sequences are composed of Changchengian to Lower Permian limestone, marlstone, and dolomite. The Middle Ordovician Majiagou Formation is widely developed in the Handan–Xingtai iron district and is mainly composed of limestone and marlstone. Based on previous petrological studies, the Majiagou formation can be divided into six units (Zhang et al. 2013), of which the first, third, and fifth units are mostly marlstone, and the second, fourth, and sixth units consist of limestone with a development of Fe mineralization (Fig. 1b). These cover sequences were folded, intruded by early Cretaceous intermediate-acidic pluton and dikes. The early Precambrian metamorphic basement outcrops occur to the north 40 km in the study area (Li et al. 2013; Sun et al. 2014).

Mesozoic magmatic rocks intruding the Precambrian basement as well as the younger sedimentary cover sequence are in a major NNE-trending magmatic belt (Fig. 1b, Shen et al. 2013a; Wang et al. 2006). The intrusive rock types include hornblende gabbro, diorite, monzodiorite, monzonite, syenite, syenogranite, and few gabbroic diorites, lamprophyre, and diorite dikes (Zheng et al. 2007a). These mafic-intermediate intrusions were emplaced between 137 and 125 Ma (discussed as below), exhibiting high $Mg^{\#}$ and the isotopic signature of EMI (Zhang et al. 2014; Wang et al. 2006; Peng et al. 2004; Shen et al. 2013a; Qian and Hermann 2010).

Deposit geology

The Pingshun deposit covers an area of 15 km^2 and is structurally controlled by regional folding series and the NE–NNE-trending magmatic belt (Fig. 1c). Surface exposure of the Pingshun deposit was originally discovered in 1954. Extensive exploration conducted by Shanxi Geological Survey and North China Geological Survey after 1954 has defined a reserve of 10.2 million tons of Fe grading 21–61%, of which more than 50% of total reserves with grades higher than 45%. A series of folds and faults trending NE–NNE are widespread in the study area (Fig. 2). The faults and folds generally parallel with the two belts of intrusions. The faults strike NE–NNE, dip NW 50–78°, and extend 6–20 km, rarely up to 200 km (Fig. 1c). The occurrence of plutons in the core along strike of the folding indicates that the cover sequence was folded at about the same time during magma emplacement (Fig. 2; Zhang et al. 2013). The igneous intrusions in the Pingshun deposit are distributed along an NNE-treading zone (approximately 50 km long by 0.5–1.4 km wide). These intrusions are divided into two belts (left and right) based on spatial outcropping patterns. The largest magmatic belt, the left magmatic belt, controls more than 90% iron ore bodies in the Pingshun deposit. The overall distribution of the ore bodies and skarns is strictly controlled by the folding and the morphology of the contact between the intrusions and Middle Ordovician carbonate, which is well illustrated by its fellows: (1) intrusions along the core of folding, (2) skarn rocks usually developed along the contact of intrusions and second unit of the Majiagou Formation and are featured by banded structure developed parallel to the stratiform layer of limestone, and (3) ore bodies often occurred as banded bodies associated with skarn rocks or as veins along fracture of wall rocks (Fig. 2).

The two magmatic intrusion belts mainly consist of diorite–monzodiorite, hornblende–diorite, and olivine-bearing hornblende gabbro (Fig. 1c). Diorite–monzodiorite with hypidiomorphic granular texture consists of plagioclase (50~70 wt%), hornblende (20~40 wt%), K-feldspar (3~20 wt%), and quartz (2~10 wt%), with minor apatite, zircon, and magnetite. The plagioclase is characterized by the typical resorbed Ca-rich core (An = 56–91) with irregular embayment in shape and surrounded by euhedral Na-rich zoned mantle (An < 27) (Zhang et al. 2014). The olivine-bearing hornblende gabbro with poikilophitic texture contains plagioclase (28~48 wt%), clinopyroxene (15~25 wt%), hornblende (10~25 wt%), olivine (5 wt%), biotite (2~5 wt%), and magnetite (2~5 wt%), with minor or trace amounts of spinel, zircon, and ilmenite, and contains dunite xenoliths (Xu et al. 2010c; Zhang et al. 2014). Clinopyroxene occurs as anhedral and was enclosed by anhedral plagioclase. Olivine and clinopyroxene with a typical reaction rim are composed of fine hornblende, biotite, and coarse magnetite (Zhang et al.

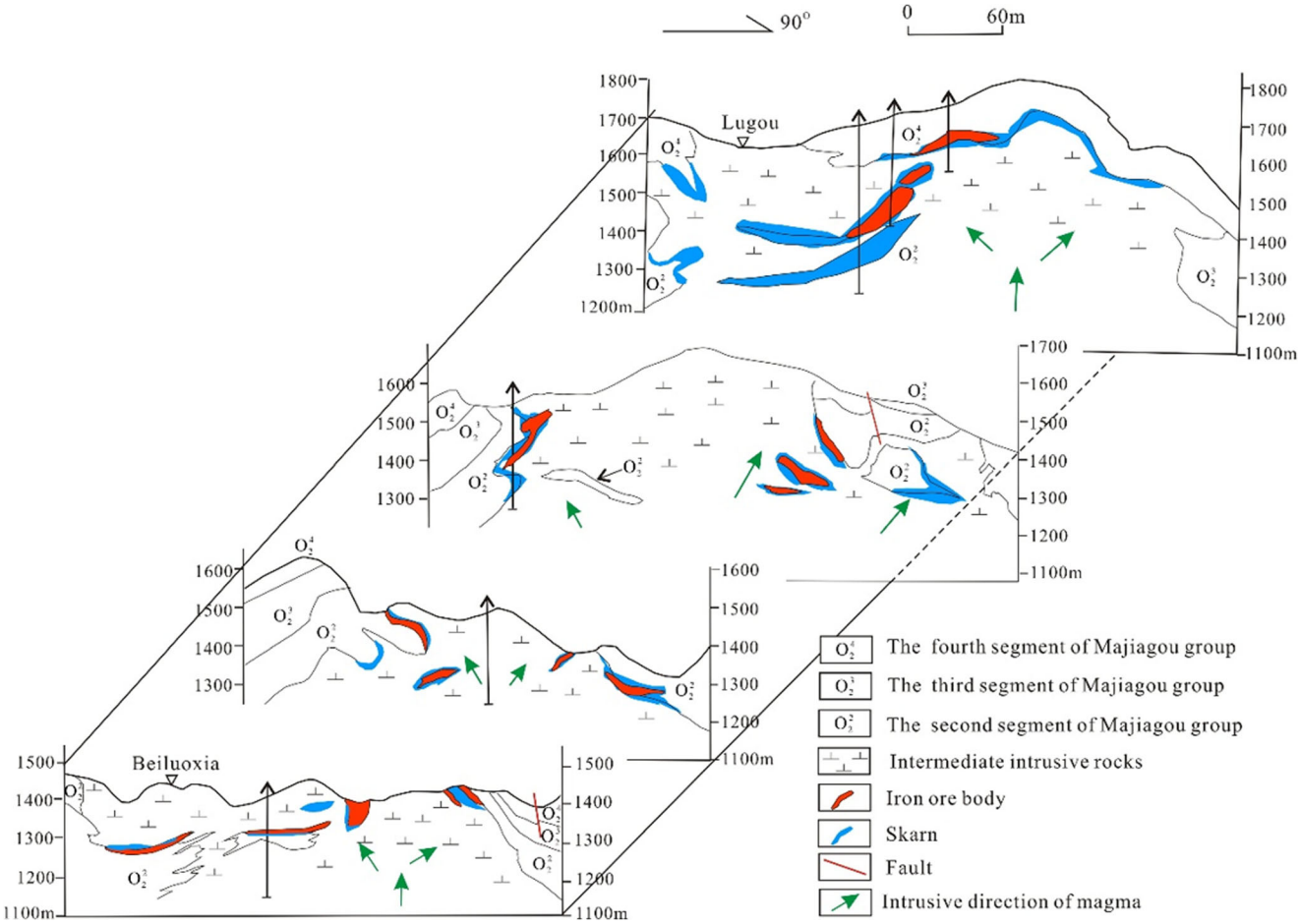

Fig. 2 Geological cross-section along exploration routes in the Pingshun deposit

2014). The fine-grained hornblende diorites consist of hornblende (50~75 wt%), plagioclase (20~40 wt%), clinopyroxene (5 wt%), biotite (2~5 wt%), and accessory minerals such as zircon and magnetite.

The ore bodies in the Pingshun deposit are developed along the contact between diorite–monzodiorite and carbonate rocks (Figs. 1c and 2). The Pingshun deposit consists of five major economic ore blocks (e.g., Beiluoxia, Lugou, Houman, Shuigou, and Jiaojiepo; Fig. 1c), in which ore bodies occur as lamina, lens, and vein shaped (Fig. 2). The individual ore bodies are generally 4~20 m thick and 100 to > 950 m long. The ore bodies dip at ~ 10° to 60° to the west or east depending on the local structure and contain an average of ~ 45 wt% Fe_3O_4.

The ore minerals are predominantly magnetite and pyrite with minor pyrrhotite, chalcopyrite, ilmenite, and arsenopyrite. The gangue minerals are mainly diopside, calcite, prehnite, garnet, epidote, and tremolite with minor biotite, chlorite, and hornblende. The ore shows various forms including dense massive (Fig. 3a), banded (Fig. 3b, c), disseminated (Fig. 3d), veined (Fig. 3e), and veinlet structures (Fig. 3f). Most of the contacts of intrusion and wall rock are sharp (Fig. 3g) with minor occurrence of typical transitional contacts in a few places.

The alteration related to iron mineralization is widespread in the mining area and consists of skarn and marble. The alteration exhibits clear zone from intrusive rocks to wall rock (Figs. 3h–i and 4): albite diorite → albitite → diopside + prehnite + tremolite + andradite → magnetite ± pyrite ± chalcopyrite → marble + epidote + calcite (Zhang et al. 2010). Alteration mainly occurs in the contact of diorite–monzodiorite and Middle Ordovician strata (Fig. 4), producing calc-silicates including albitization (Fig. 3i) and prograde and retrograde skarn. The albite zone is formed from albitization of diorite–monzodiorite (with Fe removal) relative prior to the early dry skarnization stage. The albitization of diorite–monzodiorite can be distinguished by the mineralogical and geochemical characteristics. The altered igneous rocks have lower dark-colored minerals (amphibole, pyroxene) and Fe, Mg content, higher Na and Al than unaltered rocks (Zhang et al. 2010, 2013). Primary plagioclase is surrounded by the secondary albite (Fig. 3k) and amphibole is replaced by the epidote (Zhang et al. 2013; Fig. 3l). Prograde skarn (anhydrous skarn) mainly consists of diopside and garnet (Fig. 3h, j). Retrograde skarn (hydrous skarn) consists of a mixture of prehnite, epidote, chlorite, actinolite, biotite, magnetite,

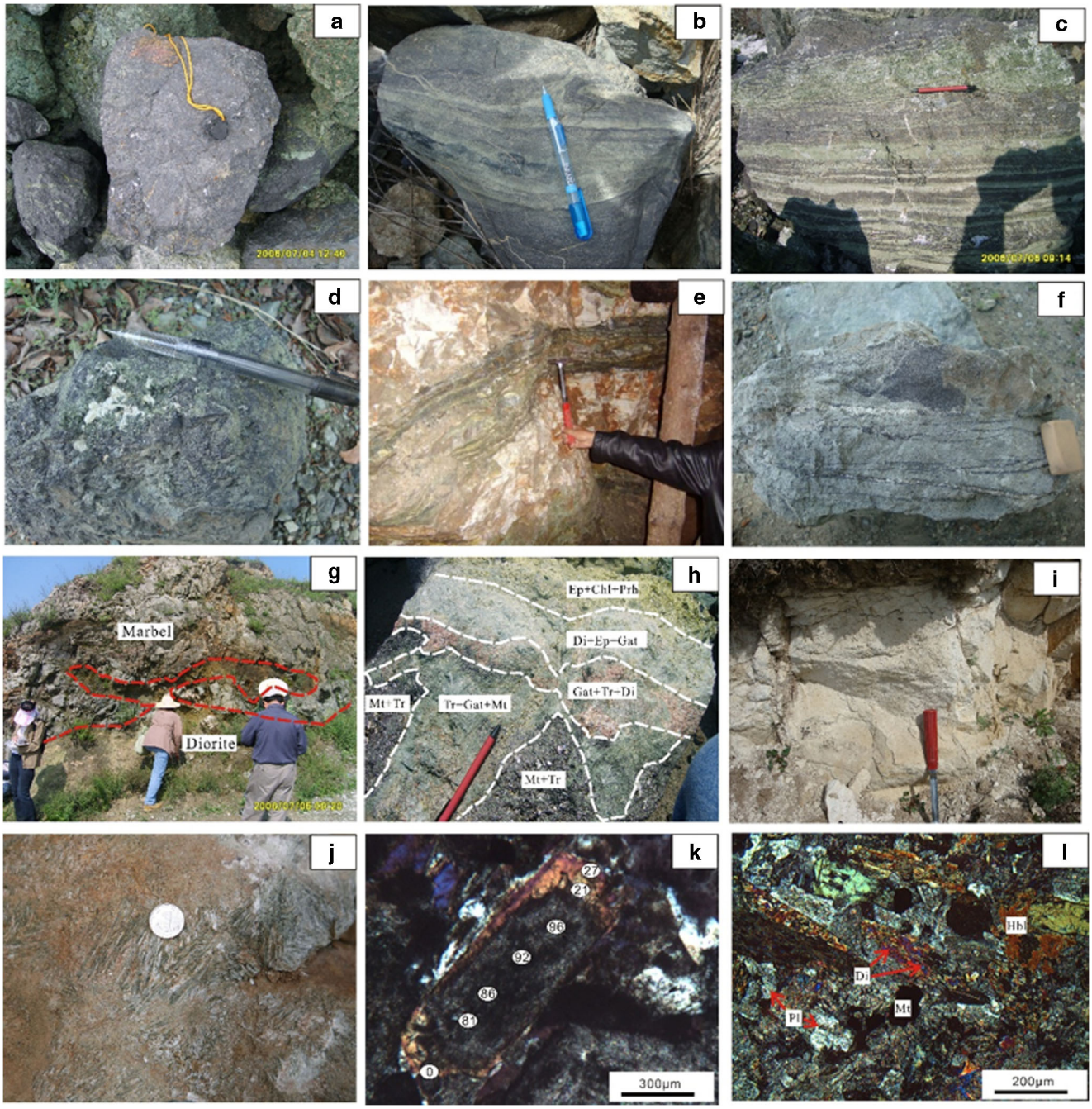

Fig. 3 Representative photos in the Pingshun deposit. **a** Ore with dense massive structure. **b**, **c** Banded ore with primary stratification. **d** Disseminated ore. **e** Ore-bearing skarn occurs as veins within marble. **f** Ore veinlet crosscutting skarns. **g** The contact between diorite and marble. **h** Alteration zones with representative minerals. **i** Albitization of diorite. **j** Diopside zone. **k** Plagioclase was surrounded by the albite. **l** Hornblende is replaced by the diopside. Ep, epidote; Chl, chlorite; Prh, prehnite; Di, diopside; Gat, garnet; Tr, tremolite; Mt, magnetite; Hbl, hornblende; Pl, plagioclase

pyrite, and chalcopyrite (Fig. 3h; Chen et al. 2016). Additionally, carbonate alteration is also developed in this area and overprints the early ablitization and consist of calcite with a minor amount of quartz and pyrite.

Based on the detailed field investigation and petrographic observation, three stages of skarn formation and ore-forming have been recognized (pre-ore, main ore, and post-ore), with a fourth supergene oxidation stage. The paragenesis is illustrated in Fig. 5. The pre-ore stage contains albitization of intrusions and earliest stage of skarn formation. No sulfides were present in this stage. Initial plagioclase and K-feldspar grains from the intrusions were albitized into albite, during which processes the mica and hornblende were disintegrated (Zhang et al. 2013). Garnets

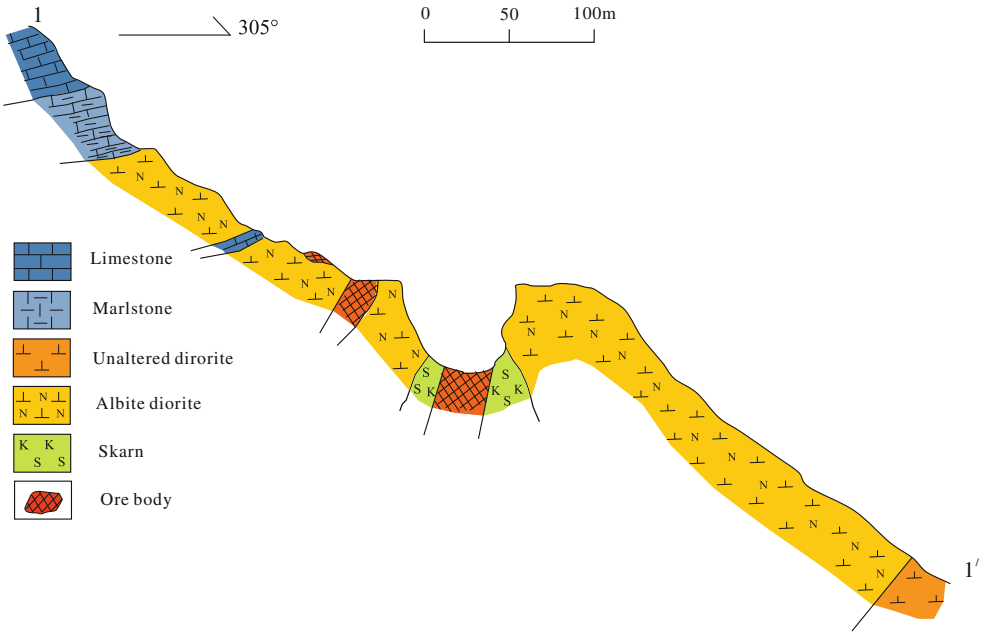

Fig. 4 Geological cross-section showing the ore bodies and zoning of skarns in the Pingshun deposit (location shown in Fig. 1c)

minerals	Pre-ore stage		Main-ore stage	Post-ore stage	Supergene stage
	Albitization	Skarn			
Albite					
Diopside					
Scapolite					
Forsterite					
Humite					
Andradite					
Prehnite					
Tremolite					
Megnetite					
Epidote					
Pyrite					
Biotite					
Chlorite					
Actinolite					
Pyrite					
Chalcopyrite					
Calcite					
Quartz					
Limonite					
Malachite					
Azurite					

Major minerals (5-100%)
Minor minerals (1-5%)
Trace minerals (<1%)

Fig. 5 Mineral paragenesis for the Pingshun skarn iron deposit

and epidotes occur as medium- to coarse-grained euhedral to subhedral crystals and are mainly products of the earliest stage of skarn deformation. The main ore stage is characterized by the occurrences of an assemblage of hydrous silicate minerals (e.g., prehnite, chlorite, actinolite, biotite, and epidote), Fe-oxides (magnetite), Cu-Fe sulfides (pyrite, chalcopyrite), and quartz. The post-ore stage is featured by the alteration of silica and carbonate, producing quartz and calcite with few Cu–Fe sulfides. The supergene stage is characterized by the occurrence of secondary hematite and malachite, which are products of replacement of magnetite and chalcopyrite, respectively, during oxide environment.

Sampling and analytical methods

Zircon U–Pb dating

In order to determine the age of skarn-related magmatic rocks, two representative samples (sample B035 and LG01) of the magmatic intrusions were selected for zircon separation and U–Pb dating. Samples B035 (diorite) and LG01 (olivine-bearing hornblende gabbro) were collected from unaltered intrusion away from iron ore bodies and alteration (Fig. 1c).

Zircons were separated using conventional heavy liquid and magnetic techniques. Representative zircon grains were handpicked under a binocular microscope, mounted in epoxy resin disks, and then polished and gold-coated. Zircons were examined under transmitted and reflected lights and then imaged by cathodoluminescence (CL) using a Gatan MonoCL3+. U–Pb isotope analyses of zircon from samples were performed using the SHRIMP II at the Institute of Geology, Chinese Academy of Geological Sciences. Details of the analytical procedures for zircon using the SHRIMP have been described by Williams and Claesson (1987) and Compston et al. (1984). During the SHRIMP analysis, spot size was 25–30 μm. Each spot was limited for 3–4 min to remove contamination on the surface. The mode of peak-jumping scanning was adopted and nine ion beam peaks, including Zr_2O^+, $^{204}Pb^+$, $^{207}Pb^+$, $^{208}Pb^+$, U^+, Th^+, and UO^+, were recorded. The average value from seven scans was recorded for each spot. Element fractionation during ion emission of zircon was used to monitor the analytical conditions relative to the RSES reference TEMORA 1 (417 Ma, Black et al. 2003). In order to ensure the reliability of the results, the standard sample was measured once for every three spots to monitor the stability of the instrument (Table 1). The data processing was conducted using the SQUID1.03 and Isoplot/Ex2.49 program of Ludwig (2001a, b).

Fluid inclusions

Five samples were collected from surface exposure in the Jiaojiepo block for fluid inclusion microanalyses in this study. The locations of the samples are shown in Figs. 1c and 6. All five samples exhibit very weak deformation. Fluid inclusions (FIs) in skarn are usually minute (3–10 μm), most of them are pseudosecondary (intragranular), and some occur as clusters or isolated (Fig. 7). More than 10 polished thin units were prepared from these samples for optical examination, of which 6 thin units were chosen for further microthermometry. FI microthermometry was conducted at the Key Laboratory of Western Mineral Resources and Geological Engineering Ministry of Education, Chang'an University using a Linkam THMSG 600 heating-cooling stage (− 198 to 600 °C). Synthetic FIs were used to calibrate the stage to ensure the accuracy of measurements. Temperature accuracy is ± 0.5 °C during −120~− 70 °C, ± 0.2 °C during − 70~+ 100 °C, and ± 2 °C during + 100~+ 500 °C. Heating/freezing rate is 5~10 °C/min, then reduced to 2 °C/min to emulate the phase transformation. Fluid inclusion salinities were estimated in terms of the reference data of Bodnar (1993) and Sterner et al. (1988) for the NaCl–H_2O system. Microthermometry data are summarized in Table 2.

Trace elements of ores

Five ore samples for trace element analyses were collected from outcrops and drill cores within Beiluoxia, Lugou, and Jiaojiepo blocks (Fig. 1c), covering dense massive, banded, and disseminated ores. Analyses were conducted using ICP-MS at the Key Laboratory of Western Mineral Resources and Geological Engineering Ministry of Education, Chang'an University. The analytical procedures applied were similar to those described by Shen et al. (2012).

S–Pb–H–O isotopes

The samples were collected from both surface exposures (Fig. 6) and drill core in the Beiluoxia, Lugou, and Houman blocks for isotopic analyses. Sulfide, magnetite, garnet, and diopside were carefully handpicked under a binocular microscope after the samples had been crushed, cleaned, and sieved to 40~60 mesh, resulting in a separate of 99% pure minerals.

Sulfur isotopes were determined at the Geological Analysis and Research Centre of Nuclear Industry of China (GARCNIC). Pyrite samples were first treated with a carbonate–zinc oxide semidissolved technique to separate pure $BaSO_4$, and then final SO_2 samples were prepared with a V_2O_5 oxidation technique. The samples were conducted using a MAT-253 EM mass spectrometer and the results are expressed in the international standard CDT with analysis accuracy better than ± 0.2‰.

Table 1 SHRIMP U-Pb isotopic analysis data for zircon grains from the Pingshun intrusions

Spot	$^{206}Pb_c$ ($\times 10^{-6}$)	U ($\times 10^{-6}$)	Th ($\times 10^{-6}$)	$^{232}Th/^{238}U$	$^{206}Pb^*/$ ($\times 10^{-6}$)	$^{207}Pb^*/^{206}Pb^*$	1σ	$^{207}Pb^*/^{235}U$	1σ	$^{206}Pb^*/^{238}U$	1σ	$^{206}Pb/^{238}U$ (Ma)	1σ
B035													
1	2.55	113	155	1.42	1.89	0.0709	9.9	0.186	10.0	0.01902	2.9	121.5	3.4
2	3.55	157	222	1.47	2.77	0.0487	19.0	0.134	19.0	0.01987	2.8	126.8	3.5
3	1.22	275	405	1.52	4.81	0.0554	8.4	0.154	8.8	0.02011	2.5	128.3	3.2
4	0.00	326	535	1.70	5.59	0.0560	3.3	0.1540	4.1	0.01996	2.4	127.4	3.1
5	1.97	359	672	1.93	6.05	0.0526	10.0	0.139	10.0	0.01922	2.4	122.7	3.0
6	1.84	273	440	1.66	4.75	0.0398	13.0	0.109	13.0	0.01986	2.5	126.8	3.2
7	4.67	197	346	1.82	3.44	0.029	37.0	0.077	37.0	0.01937	3.1	123.7	3.8
8	4.18	124	169	1.41	2.20	0.041	28.0	0.113	29.0	0.01985	3.1	126.7	3.8
LG01													
1	0.54	556	747	1.39	9.09	0.0533	3.3	0.1389	3.9	0.01892	2.1	120.8	2.5
2	0.83	510	881	1.78	8.53	0.0462	5.3	0.1229	5.7	0.01930	2.2	123.2	2.6
3	1.17	601	926	1.59	10.2	0.0507	4.9	0.1372	5.3	0.01963	2.1	125.3	2.6
4	0.71	667	759	1.18	11.4	0.0500	4.7	0.1366	5.4	0.01982	2.5	126.5	3.2
5	0.30	499	926	1.92	8.37	0.0509	3.7	0.1366	4.3	0.01947	2.1	124.3	2.6
6	1.52	466	534	1.18	7.66	0.0431	9.0	0.112	9.3	0.01885	2.2	120.4	2.6
7	1.40	637	760	1.23	11.2	0.0469	7.7	0.130	8.0	0.02019	2.2	128.8	2.8
8	0.96	490	716	1.51	8.19	0.0456	6.4	0.1211	6.8	0.01928	2.1	123.1	2.6
9	1.63	619	619	1.03	10.2	0.0468	7.5	0.1221	7.8	0.01894	2.1	121.0	2.5

Pb_c and Pb* represent the common and radiogenic portions, respectively. Pb*: corrected for common ^{204}Pb using measured ^{204}Pb. All errors are 1σ

Lead isotopic compositions were also determined at the GARCNIC. Samples were first dissolved with three common acids. Pb was separated from the treated samples using a resin exchange technique. The evaporated dry samples were analyzed using a MAT-261 mass spectrometer for which 1 μg Pb yields an accuracy of < 0.05 and 0.005% for $^{204}Pb/^{206}Pb$ and $^{208}Pb/^{206}Pb$, respectively.

Oxygen and hydrogen isotope composition were completed in the Stable Isotope Laboratory, Institute of Mineral Resources, Chinese Academy of Geological Sciences, Beijing. The analytical procedures applied were similar to those described by Peng et al. (2016). The precision is ± 0.2‰ for both $\delta^{18}O$ and δD based on repeatability analyses. Oxygen and hydrogen isotope compositions are expressed in per mille relative to Vienna-Standard Mean Ocean Water (V-SMOW).

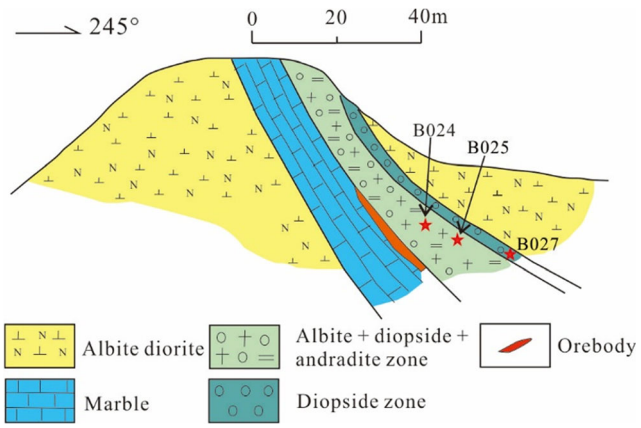

Fig. 6 Distribution of skarns and location of samples in the Beiluoxia district of Pingshun deposit

Results

Zircon U–Pb ages

The zircons from the samples (LG01 and B035) exhibit similar morphology, mostly euhedral and up to 70–140 μm in length with aspect ratios of about 1:1.5 to 1:3. The zircon grains without a structure on CL images show prismatic or irregular shape (Fig. 8). Zircons from samples LG01 and B05 have Th/U = 1.03–1.92 and 1.41–1.93, respectively, indicating a magmatic origin (Lee et al. 1997; Black et al. 2003). The model $^{206}Pb/^{238}U$ ages of nine spots vary from 121.5 to128.33 Ma, yielding a weighted mean $^{206}Pb/^{238}U$ age of 123.4 ± 1.7 Ma (MSWD = 1.10) (Fig. 8a; Table 1). Eight SHRIMP spot measurements of zircons from sample B035 define a tight cluster on a concordia diagram, yielding a weighted mean $^{206}Pb/^{238}U$ age of 125.5 ± 2.3 Ma (MSWD = 0.58) (Fig. 8b). These dating results could be interpreted as the crystallization age of the Pingshun intrusions.

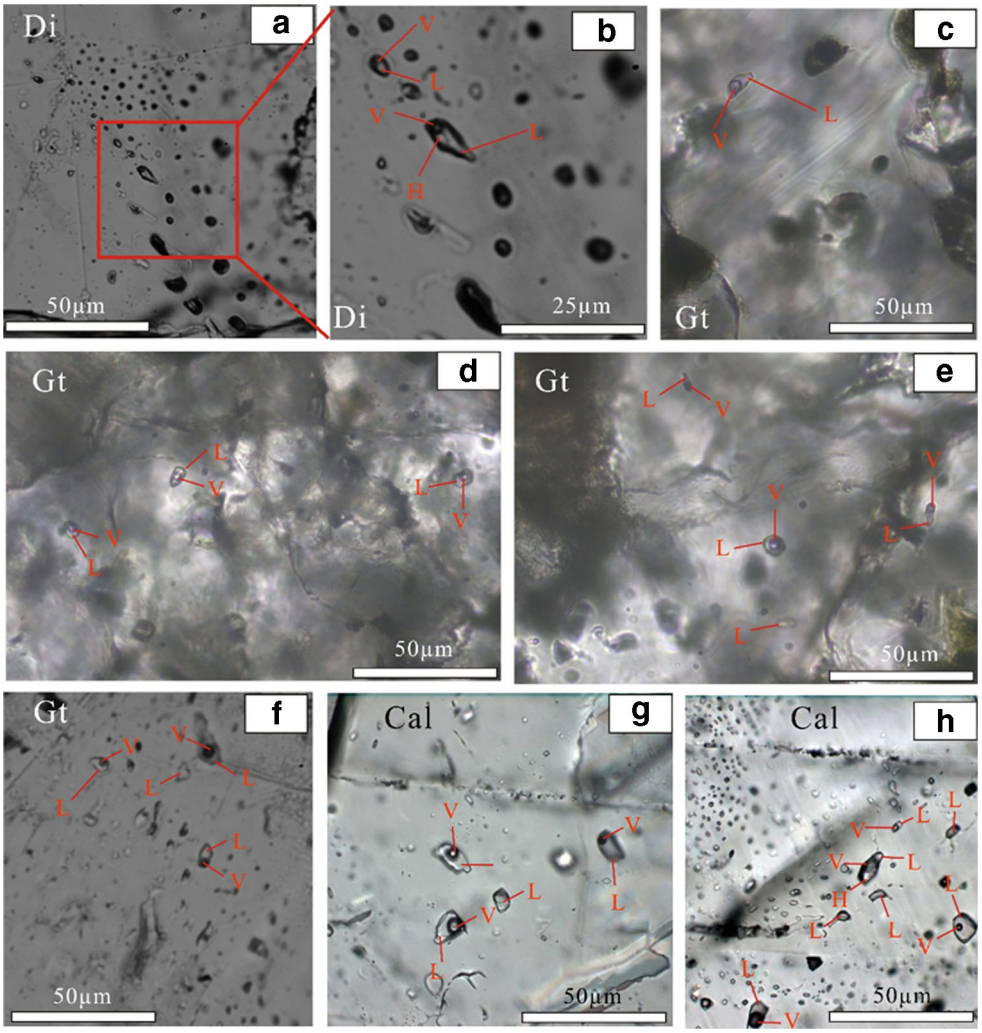

Fig. 7 Representative photomicrographs of different types of fluid inclusions from multiple stages. **a**, **b** Three-phase (type 1) and 2-phase (type 2) inclusions in diopside (sample B204) occur as clusters. **c**, **d** Two-phase inclusions in garnet (sample B207) exhibit isolated shapes. **e**, **f** Two-phase inclusions occur as clusters and isolates and coexist with rare pure liquid inclusions in garnet (sample B207). **g**, **h** Two-phase inclusions coexist with rare pure liquid inclusions in calcite (sample B205). Note that calcite occurs as vein in samples B205 and B207. V, aqueous vapor bubble; L, aqueous liquid phase; H, halite; Di, diopside; Gt, garnet; Cal, calcite

Microthermometry of fluid inclusions

Primary FIs hosted in garnet, diopside, and calcite were identified. Three major types of primary FIs were identified based on their occurrence, nature, and phase transformation during cooling and heating processes (Goldstein and Reynolds 1994; Li et al. 1989). The type 1 FIs are 3-phase inclusions containing a vapor bubble, an aqueous liquid, and daughter minerals (Fig. 7b, h); type 2 FIs are two-phase inclusions consisting of a vapor bubble and an aqueous liquid (Fig. 7b–h); type 3 FIs are pure liquid inclusions (Fig. 7b, h). Type 1 FIs show subrounded, elongated shapes and occur as clustered or isolated in diopside and calcite minerals, but type 1 FIs within calcite were not observed in this study compared with Li et al. (1989). Type 1 FIs range in size from 5 to 30 μm (Fig. 7b, h). FIs hosted in diopside are almost entirely type 1 with minor type 2. Type 2 FIs in garnet and calcite (Fig. 7c–h) exhibit isolated and irregular shapes and are generally 5–20 μm in diameter. The pure liquid FIs (type 3) were mainly hosted in calcite and garnet grains and show subrounded, tubular, and irregular shape (Fig. 7e–h). The coexistence of type 2 and 3 FIs is observed in calcite and garnet grains (Fig. 7e, f).

Fls hosted in diopside, garnet, and calcite record the physicochemical information of the ore-forming fluids (Fig. 9a, b). Type 1 FIs hosted in diopside grains have a homogenization temperature ranging from 486 to 679 °C (averaging 574 °C) and from 240 to 260 °C in calcite, corresponding to salinities from 39.8 to 77.6 wt% NaCl equiv. (averaging 61.7 wt% NaCl equiv.) and 29.7 to 35.5 wt% NaCl equiv. The homogenization temperature of type 2 has a wider range from 365 to 496 °C in garnet and from 162 to 295 °C in calcite, corresponding to salinities of 11.8–17.6 and 6.7–21.1 wt% NaCl equiv. The daughter minerals in type 1 FIs hosted in diopside were observed and measured by Li et al. (1989) and are halite, sylvite, hematite, and gypsum.

Table 2 Microthermometric data of different types of fluid inclusions from the Pingshun intrusions

Stage	Host mineral	FI type	Sample	Number	FI size (μm)	Tm_{ice} (°C)	Td_{solid} (°C)	Th_{TOT} (°C)	Salinity (wt% NaCl)
Pre-ore	Diopsite	1	B024	5	5–30	/	516 to 519	516 to 528	61.8 to 63.5
		1	B293*	4	5–30	/	515 to 622	515 to 622	58.1 to 71.8
		1	B405*	2	5–30	/	551 to 602	551 to 602	62 to 69
		1	B285*	6	5–30	/	327 to 587	486 to 587	39.8 to 69.9
		1	B271*	12	5–30	/	450 to 659	540 to 679	50.8 to 77.6
	Garnet	2	B027	6	5–30	− 13.8 to − 8.1	/	365 to 496	11.8 to 17.6
Post-ore	Calcite	1	B294*	3	5–30	/	146 to 260	240 to 260	29.7 to 35.3
		2	B205	9	10–30	− 18.2 to − 4.2	/	162 to 295	6.7 to 21.1
		2	B207	9	10–30	− 12.8 to − 7.5	/	191 to 294	11.1 to 16.7

FI = fluid inclusion; Tm_{ice} = ice melting temperature; Td_{solid} = dissolution temperature of solid; Th_{TOT} = total homogenization temperature
*Data from Li et al. (1989)

Trace elements of ores

Although the samples of different ore types (Table 3) have lower total rare earth elements (total REE, 2.10–35.56 ppm) compared with the Pingshun intrusions (59.54–139.14 ppm; Zhang et al. 2014), they exhibit coherent primary mantle-normalized trace element patterns (Fig. 10a; Sun and McDonough 1989) and chondrite-normalized REE patterns (Fig. 10b; Taylor and McLennan 1985). The Pingshun iron ore samples are characterized by enrichment of Sr and La and lower Nb and Ta. They also show slight enrichment of light rare earth elements (LREEs) relative to the heavy rare earth elements (HREEs, LREEs/HREEs = 4.48–14.75, Table 3).

Mineral isotopic composition

Pyrite have homogeneous $\delta^{34}S$ values varying from 12.5 to 17.4‰, with an average of 15.0‰ (Fig. 11). The $\delta^{34}S$ values are higher than the majority of known magmatic hydrothermal deposits (− 3 to 1‰; Hoefs 2009), but lower than that of the sedimentary gypsum in the Handan–Xingtai iron district (> 22‰; Shen et al. 2013b) (Fig. 11).

The lead isotopic compositions of the 11 pyrite samples from the Pingshun deposit are characterized by large variation in $^{206}Pb/^{204}Pb$, $^{207}Pb/^{204}Pb$, and $^{208}Pb/^{204}Pb$, ranging from 17.26 to 19.03 (mean = 18.12), 15.42 to 15.69 (mean = 15.54), and 37.29 to 39.76 (mean = 38.78), respectively, and exhibit clear linear correlations (Fig. 12). As shown in Fig. 12, the lead isotopic compositions of 11 different types of sulfides are similar to those of the Pingshun intrusions and sulfides from the Handan–Xingtai iron district (HXID).

Equilibrium fluid oxygen isotopic composition of garnet, diopside, and magnetite was calculated using the fractional equilibrium formulae proposed by Taylor (1976), Zheng et al. (1995), and Zheng and Chen (2000). The crystallization temperatures of garnet and diopside were obtained from the microthermometric results of the fluid inclusions, whereas the crystallization temperatures of

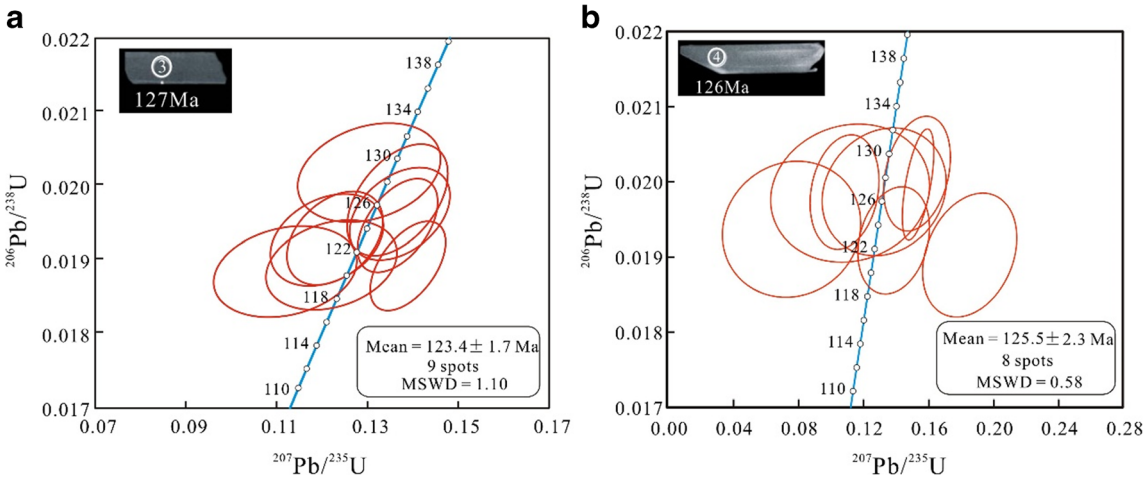

Fig. 8 **a**, **b** SHRIMP zircon U–Pb concordia diagram and $^{206}Pb/^{238}U$ average age for olivine-bearing hornblende gabbro (LG01) and diorite (B035). The representative CL images of analyzed zircon grains with no structure are shown

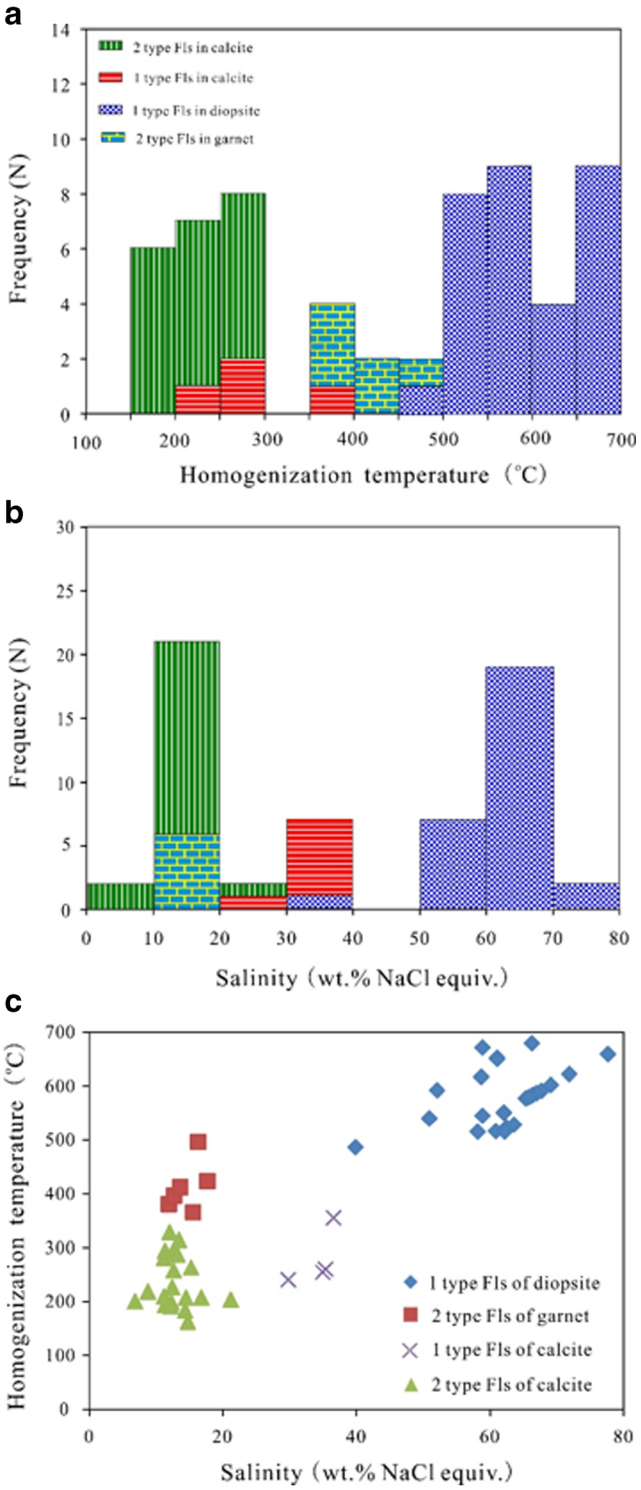

Fig. 9 Data on fluid inclusions in minerals for pre-ore and post-ore stage skarns from the Pingshun deposit. Frequency histograms of final homogenization temperature (**a**), salinities (**b**), and homogenization temperature vs. salinities diagram (**c**), for fluid inclusions from the Pingshun deposit

magnetite were estimated by using the homogenization temperatures of fluid inclusions hosted in garnet. The $\delta^{18}O_{Mineral}$ values are 6.7 to 8.0‰ for garnet with calculated $\delta^{18}O_{H2O}$ values of 9.5–10.8‰, the $\delta^{18}O_{Mineral}$ value is 8.7‰ for diopside with calculated $\delta^{18}O_{H2O}$ values of 10.8‰, and $\delta^{18}O_{Mineral}$ values are 2.6 to 6.2‰ for magnetite with calculated $\delta^{18}O_{H2O}$ values of 9.8–13.4‰. The δD values are in the range of −106 to −86‰ for garnet ($N = 3$) and −90‰ for diopside.

Discussion

Timing of mineralization

The skarn deposits were formed by alteration of intermediate-mafic magma with carbonates (Seltmann and Porter 2005; Seltmann et al. 2014; Shen et al. 2015), indicating that the timing of mineralization is well coincident with the time of emplacement of the associated magmatic intrusions. The distribution of ore bodies and skarn alteration in the Pingshun deposit are strictly controlled by the morphology of the contact between altered diorite–monzodiorite and Middle Ordovician carbonates (Figs. 2, 4, and 6), suggesting the time of emplacement of altered diorite is consistent with the timing of mineralization in Pingshun area. This suggestion is also supported by previous researchers on other iron deposit (e.g., Xishimeng skarn iron deposit) in the adjacent area in the Handan–Xingtai iron district (Peng et al. 2004; Zheng et al. 2007b). Peng et al. (2004) documented that the SHRIMP zircon U–Pb ages of albitization of diorite associated with iron mineralization were 137 ± 2 Ma, which is similar with the age of iron mineralization measured by the $^{40}Ar/^{39}Ar$ age of phlogopite (137 ± 2 Ma). The new data for gabbro and diorite (123.4 ± 1.7 Ma for gabbro and 125.5 ± 2.3 Ma for diorite) might also represent the timing of mineralization in Pingshun. Hence, it is confident to conclude that both magmatism and mineralization in the Pingshun deposit took place at around 125–123 Ma.

Source of metal and ore-forming fluid

In this study, the $\delta^{34}S$ values of pyrite separated from different types of iron ores in the Pingshun deposit vary from 12.5 to 17.4‰ with a median value around 15.0‰ (Table 4). The narrow variation range is similar to other skarn iron deposits in the Handan–Xingtai iron district reported in other studies (Shen et al. 2013b; Zheng et al. 2007a), but higher than many typical magmatic hydrothermal deposits (−3 to 1‰; Hoefs 2009; Qu et al. 2007; De Hoog et al. 2001) and other skarn Zn–Pb deposits (−6.7 to 14.0‰, Mei et al. 2015; Xu et al. 2010a), which strongly excludes the possibility of single magmatic origin. Moreover, in Fig. 11, the data points of samples from the Pingshun deposit fall in between the intrusions and sedimentary gypsum in the Handan–Xingtai iron district (Shen et al. 2013b), suggesting that the sulfur of the

Table 3 The analytical results of trace elements (10^{-6}) of various ore types in the Pingshun deposit

Samples	LG11	BLX02	JGP01	LG05	LG02
Location	Lugou	Beiluoxia	Jiaojiepo	Lugou	
Lithology	Dense massive ore			Disseminated ore	Banded ore
Rb	2.45	2.08	0.74	3.75	1.78
Ba	18.97	13.01	12.93	83.12	45.71
Th	0.73	0.12	0.23	0.40	0.79
U	0.085	0.017	0.057	0.18	3.45
Ta	0.001	0.007	0.005	0.001	0.004
Nb	0.084	0.26	0.12	0.11	0.79
La	2.49	0.55	3.69	1.49	10.20
Ce	3.90	0.64	3.38	1.32	14.80
Sr	37.34	16.53	278.7	376.6	90.08
Nd	2.55	0.37	1.45	0.87	6.10
Zr	7.38	1.15	1.47	1.21	2.05
Hf	0.17	0.068	0.052	0.036	0.050
Sm	0.50	0.089	0.27	0.22	0.024
Y	2.06	0.12	0.59	1.45	3.36
Cr	10.73	6.94	5.98	3.78	2.94
Co	151.5	57.11	13.59	8.70	18.33
V	165.9	33.76	417.1	138.0	88.19
Ni	50.73	22.17	122.5	50.28	44.62
Cu	269.4	88.02	45.46	35.59	41.81
Zn	150.7	31.51	8.02	10.87	15.91
La	2.49	0.55	3.69	1.49	10.20
Ce	3.90	0.64	3.38	1.32	14.80
Pr	0.56	0.18	0.47	0.26	1.79
Nd	2.55	0.37	1.45	0.87	6.10
Sm	0.50	0.089	0.27	0.22	0.024
Eu	0.16	0.027	0.21	0.40	0.013
Gd	0.50	0.13	0.31	0.35	1.05
Tb	0.058	0.003	0.029	0.039	0.11
Dy	0.36	0.017	0.13	0.27	0.67
Ho	0.071	0.001	0.019	0.054	0.12
Er	0.23	0.014	0.065	0.14	0.35
Tm	0.030	0.002	0.007	0.018	0.047
Yb	0.24	0.065	0.070	0.11	0.25
Lu	0.038	0.015	0.010	0.022	0.036
ΣREE	11.68	2.10	10.11	5.57	35.56
ΣLREE/ΣHREE	6.64	7.50	14.75	4.48	12.48
$(La/Yb)_N$	6.99	5.69	35.53	8.82	27.29
$(La/Sm)_N$	3.2	3.9	8.8	4.2	267.3
$(Gd/Yb)_N$	1.69	1.61	3.57	2.49	3.38
δEu	0.965	0.767	2.236	4.29	0.08
δCe	0.77	0.49	0.53	0.47	0.77

Pingshun deposit has a mixture origin of magma with Middle Ordovician carbonate rocks (e.g., the Majiagou Formation).

In the $^{207}Pb/^{204}Pb$–$^{206}Pb/^{204}Pb$ and $^{208}Pb/^{204}Pb$–$^{206}Pb/^{204}Pb$ diagrams (Fig. 12), the Pingshun deposit samples show bigger variation in lead isotopic composition and demonstrate a clear linear relation. This is similar to those of the Pingshun intrusions and Beiminghe ore sulfides with slightly higher values, suggesting that the ore sulfides in the Pingshun deposit and intrusions in

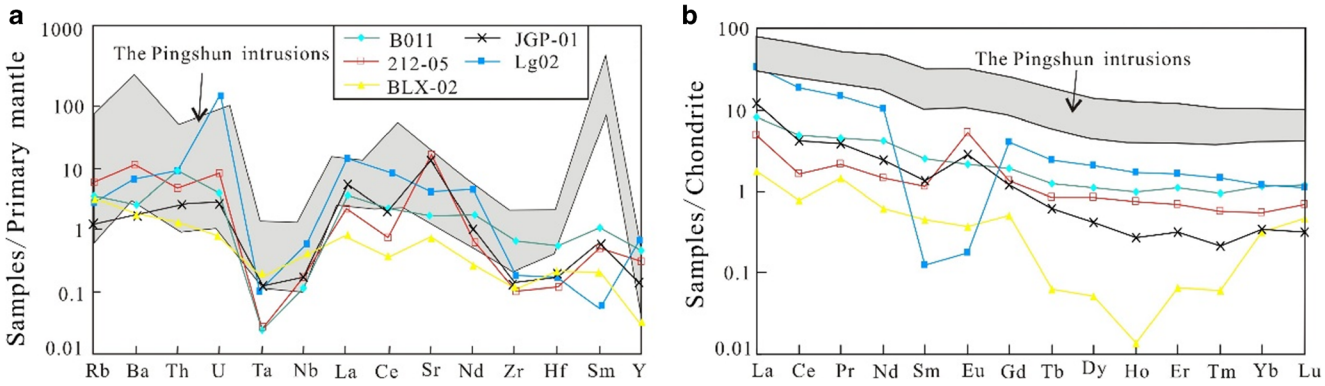

Fig. 10 **a** Plots of primitive mantle-normalized trace elements (Sun and McDonough 1989) and **b** chondrite-normalized rare earth elements (Taylor and McLennan 1985) for various ore types from the Pingshun deposit. Data for Pingshun intrusions are from Zhang et al. (2014)

the Handan–Xingtai iron district have similar lead sources, but the more crustal material might be involved during the mineralization process in Pingshun area. Additionally, the coherent chondrite-normalized REE patterns (Fig. 10b) and primary mantle-normalized trace element patterns (Fig. 10a) of ores and intrusions in Pingshun also suggest that the ore materials were derived from the magmas and additional crustal material involved during the mineralization process. This is also supported by the coexistence of diorite–monzodiorite and ore bodies (Figs. 2, 4, and 6).

In the δD (‰) vs. $\delta^{18}O_{H2O}$ diagram (Fig. 13), all data fall in the area between magmatic water and the meteoric water line and slightly under the magmatic water region, which can be explained by mixing of the magmatic fluid and meteoric water that caused the hydrogen and oxygen compositions to shift to the meteoric water line. Hoefs (2009) reported that the intense wall rock alteration can result in the loss of ^{18}O, and thus, magnetite that underwent the late alteration may yield lower $\delta^{18}O$ values. However, prograde garnet and diopside have similar $\delta^{18}O_{H2O}$ values (9.5 to 10.8‰) to, but slightly lower than, retrograde magnetite (9.8 to 13.4‰) (Fig. 12, Table 5), which is inconsistent with the argument of Hoefs (2009). This indicates that there are additional materials with high $\delta^{18}O$ values involved during alteration (Shi et al. 1983; Zhu et al. 2016). Additionally, Taylor (1976) noted that the $\delta^{18}O$ values in magnetite originated from magma vary from 1 to 4‰, while the magnetite from the different types of ores in Pingshun deposit yields much higher $\delta^{18}O$ values (9.8–13.4‰). This may also support the mixture origin of magmatic fluid with meteoric water.

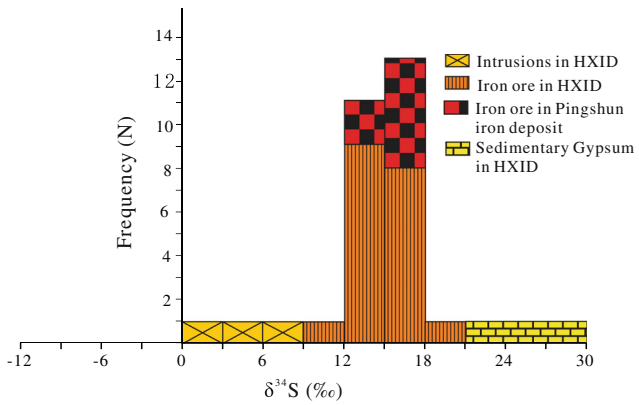

Fig. 11 Frequency histogram plot of $\delta^{34}S$ for pyrite from the Pingshun deposit. HXUD, Handan–Xingtai iron district

Evolution of ore-forming fluid

The FIs (type 1) in diopside from prograde skarn close to the albite diorite–monzodiorite (Fig. 6) were formed from hot, hypersaline brines based on our data (486–679 °C, 39.8–77.6 wt% NaCl equiv.; Fig. 9). The characteristics of higher temperatures and salinities in these fluids were previously considered as indicative features of the magmatic origin (Vallance et al. 2009; Wilkinson 2001; Kesler 2005) supported by the $\delta^{18}O$ values of diopside (10.8‰) overprinted by the magmatic fluids (Taylor 1974). However, the high temperature and high salinity fluids could result from low to moderate salinity fluids by boiling with reduced pressure or aqueous phase immiscibility (Cline 2003; Heinrich 2007), both of which are usually associated with the unroofing of a batholith (e.g., Mollai et al. 2009) in a primary boiling process. The fluid in the measured diopside samples from Pingshun deposit contains some solids of halite, sylvite, hematite, and gypsum (Li et al. 1989), indicating that the fluid in the pre-ore stage is characterized with high Na, Fe, and Cl. It is believed that the high Fe content was derived from the decomposition of hornblende and biotite during the process of albitization of diorite, which is supported by S and Pb isotopic data and the decrease of biotite and hornblende in diorite–monzodiorite close to the skarn. The presence of sylvite and gypsum as solid phase and the higher Cl content in the fluids in diopside (Li et al. 1989) reveal that the sediments of gypsum were trapped by the magmas during the emplacement process. The robust evidence for this hypotheses is that the occurrence of gypsolyte and salt-bearing marlstone in the third and sixth units of Middle Ordovician Majiagou Formation (Zheng et al.

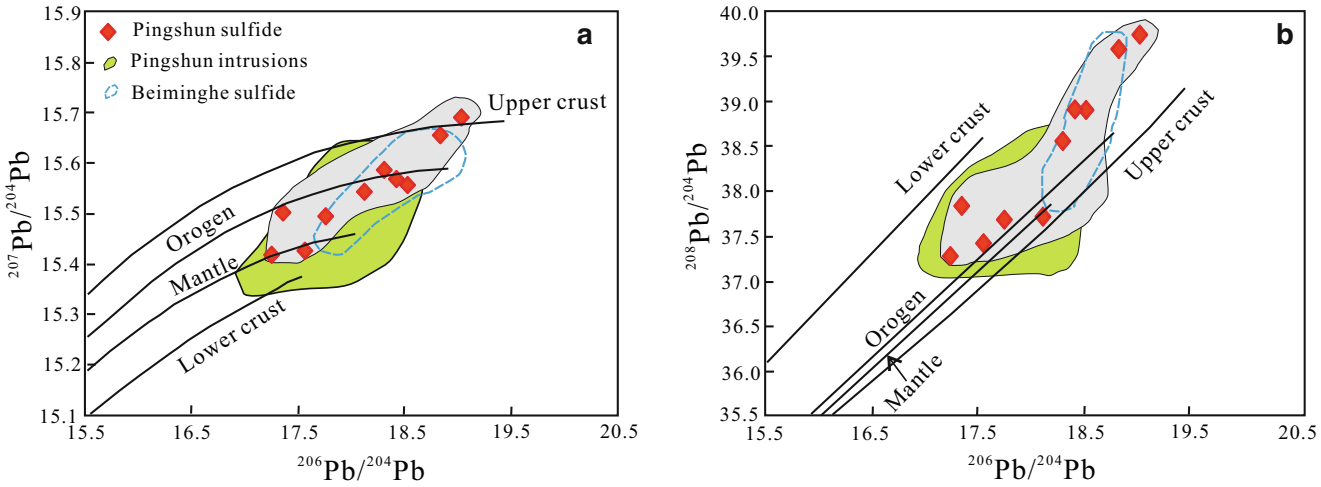

Fig. 12 Plots of $^{207}Pb/^{204}Pb$ vs. $^{206}Pb/^{204}Pb$ (**a**) and $^{208}Pb/^{204}Pb$ vs. $^{206}Pb/^{204}Pb$ (**b**) for pyrite from the Pingshun deposit. The base plots and interpretation are from Zartman and Doe (1981). Data of the Pingshun intrusions are from Zhang et al. (2014) and data of the Beiminghe sulfide is from Shen et al. (2013b)

2007a), which excludes the possibility of gypsolyte from the magmatic hydrothermal system (Luo et al. 2015).

Andradite-rich garnet is widely present in the skarn, suggesting that garnet was crystallized from ore-forming fluid under high oxygen fugacity (Hawkins et al. 2017). The FIs trapped in garnet are type 2 with homogenization temperature of 365–496 °C and salinities of 11.8–17.6 wt% NaCl equiv. The type 2 fluid inclusions in garnet have slightly lower homogenization temperature and significantly low salinity compared with type 1 inclusions trapped in diopside (Fig. 9c), indicating more additional meteoric water involved causing reduction of salinity of the fluid. Meanwhile, garnet has slightly lower $\delta^{18}O$ values than diopside (Fig. 13, Table 5), supporting this idea that there might be additional meteoric water involved during the formation of garnet. The rare occurrence of type 2 and type 3 inclusions in garnet also provides evidence of the presence of reduced pressure or secondary boiling from sudden pressure decreases (Fig. 7c–f; e.g., Zhou et al. 2017). The fluid flow in the hydrothermal system is always associated with boiling causing a decrease in temperature and pressure and an increase in salinity (Fig. 9c) within the fluid (Chen et al. 2016). This results in the decomposition of metal complexes (FeCl) and precipitation of andradite garnet and magnetite from hydrothermal fluids under high oxygen fugacity (Yardley et al. 1991; Jamtveit et al. 1993). This idea is also supported by the coexistence of type 2 and 3 FIs in garnet, which has been observed by Li et al. (1989).

Table 4 Sulfur and lead isotope composition (‰) of pyrites from skarns and ores in the Pingshun deposit

Sample	Mineral	Location	Description	$^{206}Pb/^{204}Pb$	$^{207}Pb/^{204}Pb$	$^{208}Pb/^{204}Pb$	$(^{206}Pb/^{204}Pb)_i$	$(^{207}Pb/^{204}Pb)_i$	$(^{208}Pb/^{204}Pb)_i$	$\delta^{34}S$ (‰)
LB-1	Pyrite	Lugou	Banded ore	18.301	15.551	37.936	18.125	15.542	37.732	
LB-2			Disseminated ore	17.937	15.501	37.911	17.762	15.493	37.697	
LB-25			Disseminated ore	17.741	15.433	37.643	17.568	15.425	37.433	
B09		Beiluoxia	Dance massive ore	17.542	15.51	38.085	17.365	15.501	37.851	15.4
B24			Ore-bearing skarn	19.212	15.698	39.995	19.032	15.689	39.762	17.4
B38			Disseminated ore	18.704	15.564	39.146	18.528	15.555	38.923	13.8
B43			Disseminated ore	19.015	15.663	39.837	18.836	15.654	39.603	15.5
B62			Disseminated ore	18.487	15.594	38.798	18.311	15.585	38.575	12.5
B65			Pyrite veinlet crosscutting skarn	18.601	15.576	39.156	18.424	15.567	38.929	15.2
B66			Disseminated ore with pyrite veinlet	17.432	15.425	37.507	17.258	15.417	37.289	15.0

Initial Pb isotopic ratios were calculated using the measured whole-rock Pb isotopic compositions, whole-rock U, Th, and Pb contents by assuming 125 Ma. $\Delta 7/4 = ((^{207}Pb/^{204}Pb)_i - (^{207}Pb/^{204}Pb)_{NHRL}) \times 100$; $\Delta 8/4 = ((^{208}Pb/^{204}Pb)_i - (^{208}Pb/^{204}Pb)_{NHRL}) \times 100$; $(^{207}Pb/^{204}Pb)_{NHRL} = 0.1084 \times (^{206}Pb/^{204}Pb)_i + 13.491$, $(^{208}Pb/^{204}Pb)_{NHRL} = 1.209 \times (^{206}Pb/^{204}Pb)_I + 15.627$ (Hart 1984)

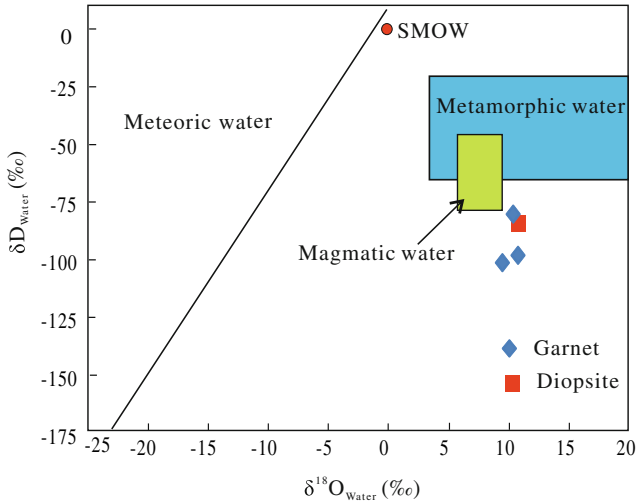

Fig. 13 δD vs. $\delta^{18}O_{H2O}$ plot in the Pingshun deposit. The base plots are from Taylor (1997)

The banded ores were cut by calcite veinlets in the Pingshun deposit (Fig. 3c) indicating that the calcite was formed later than magnetite. Therefore, fluid inclusions trapped in calcite might record the chemical composition and physicochemical condition of the post-ore–forming fluid. The type 2 and 3 FIs in calcite yield homogenization temperature ranging from 240 to 260 °C and 162 to 295 °C, with salinities of 29.7–35.3 and 6.7–21.1 wt% NaCl equiv., respectively. The significant difference of homogenization temperature and salinity of type 2 FIs between pre-ore–forming fluids (trapped by Garnet and diopside) and post-ore–forming fluids (trapped by calcite; Fig. 9c) indicates that the precipitation of magnetite was caused by the remarkable variation of fluid temperature, composition, and pH due to extensive boiling (Chen et al. 2016; Hawkins et al. 2017). The coexistence of type 2 and 3 inclusions trapped in calcite also suggests that the boiling occurred during the formation of calcite which caused a decrease in fluid temperature and an increase in salinity (Fig. 9c).

Metallogenic modeling

The results of SHRIMP zircon U–Pb dating and the spatial distribution of Pingshun intrusions show that these intrusions were emplaced at a limited range of 125–123 Ma, suggesting the later magma (olivine-bearing hornblende gabbro) was emplaced prior to the complete crystallization of early magma (diorite–monzodiorite). Later magma increased the temperature of fluids and accelerated the interaction of ore-forming fluids with carbonates and formed more than ~ 300 m thick skarns in the Pingshun area (Fig. 2). The isotopic composition of minerals and the microthermometry of FIs show that the ore-forming fluids were originated from magmatic fluid mixed with additional meteoric water, gypsum, and carbonates.

Based on the above observation and reported studies (Zhang et al. 2010, 2014; Zheng 2007; Shen et al. 2013a, b; Xu et al. 2010b), we propose that the origin of the Pingshun deposit may involve a series of processes: (1) emplacement of magmas was originated from the mixing of magmas from refractory peridotite and crustal magma (Zhang et al. 2014; Xu et al. 2010c). The emplacement was accompanied by crystallization and exsolution of volatile-rich phase that formed hot and ore-bearing hydrothermal fluids (as shown in type 1 inclusion of diopside). (2) During crystallization process of magmas, the hot fluids increased in volume and interacted with the surrounding carbonate rocks. The interaction process incorporated Na, Ca, and Cl from the gypsolyte and salt-bearing marlstone into ore-bearing fluids that increased the fluid transportation ability for Fe and enhancing the capacity of Fe in ore-forming fluids and made the development of extensive skarn alteration feasible. (3) The

Table 5 Hydrogen and oxygen isotopic data of the Xi'anli iron deposits

Stage	Sample	Location	Mineral	δD_{SMOW} (‰)	$\delta^{18}O_{V\text{-}SMOW}$ (‰)	Th (°C)	$\delta^{18}O_{H2O}$ (‰)
Pre-ore	B027	Lugou	Garnet	− 86	7.7	475	10.4
	B204-1		Garnet	− 106	6.7	500	9.5
	B027-1		Garnet	− 103	8.0	500	10.8
	B024-2		Diopsite	− 90	8.7	565	10.8
Main ore	P31-8	Beiluoxia	Magnetite		3.3	420	10.8
	P78-3		Magnetite		6.2	470	13.4
	P80-1		Magnetite		4.3	470	11.5
	P77-4		Magnetite		2.6	470	9.8

The temperatures of garnet and diopsite were obtained from homogenization temperature of fluid inclusions and data for magnetite was inferred from the lowest homogenization temperature of fluid inclusions in garnet. The equations used for mineral–water oxygen isotopic fractionation were as follows: $1000\ln\alpha_{garnet\text{-}H2O} = 1.22 \times 106\ T^{-2} - 4.88$ (Taylor 1976); $1000\ln\alpha_{diopsite\text{-}H2O} = 3.92 \times 106\ T^{-2} - 8.43 \times 103\ T^{-1} + 2.40$ (Zheng and Hoefs 1993); $1000\ln\alpha_{magnetite\text{-}H2O} = 2.88 \times 106\ T^{-2} - 11.36 \times 103\ T^{-1} + 2.89$ (Zheng and Chen 2000); $\delta^{18}O_{V\text{-}SMOW} = 1.03{,}086 \times \delta^{18}O_{V\text{-}PDB} + 30.86$ (Friedman and O'Neil 1977)

multistage fluid boiling causing effective changes in physico-chemical condition and the addition of meteoric water into the ore-forming fluids were considered to be key factors controlling ore precipitation (Jamtveit et al. 1993; Chen et al. 2016; Palinkaš et al. 2013).

Implication for the occurrence of numerous iron deposits in Handan–Xingtai iron district

Previous studies have revealed that the NCC has been extensively modified by tectonic and magmatic events since the Paleoproterozoic and especially during 140–110 Ma (Zhai and Santosh 2011; Wu et al. 2008; Zhang et al. 2017), as evidenced by widespread magmatism, development of large sedimentary basins, and large-scale ore deposit formation (Yang et al. 2008; Li and Santosh 2014). The time of formation of skarn iron deposits in the Pingshun and Handan areas is 125–123 and 137 Ma (Zheng et al. 2007b; Shen et al. 2015), respectively, which is consisting with the peak of 136–123 Ma for the magmatic activity in southern Taihang Mountains (Chen et al. 2008; Peng et al. 2004; Wang et al. 2006; Zheng et al. 2007b). The Sr–Nd–Pb isotopic characteristics (EMI-like) and REE features without obvious Eu anomalies of plutons from southern Taihang Mountains have been interpreted as the signature of mixing of mantle–crust magmas (Peng et al. 2004; Wang et al. 2006; Zhang et al. 2014) and the significant marks of the large-scale lithospheric destruction of the eastern block of NCC (Peng et al. 2004; Zhu et al. 2011; Zhang et al. 2014). A comparison with composition of igneous rocks, lithosphere thickness and Fe reserves in the northern TaihangMountains, there are more mafic intrusions, higher lithosphere thickness and larger Fe reserves in the southern Taihang Mountains of the southern Taihang Mountains (Zhang et al. 2014, 2017; Li and Santosh 2014; Shen et al. 2013a, b), suggesting that the formation of the skarn iron deposits was mainly controlled by the component of mantle materials in magmas. With more mantle materials involved in magmas, there is a large addition of Fe to the magmas, which significantly increases the capacity of Fe in magmas and lifts the possibility of Fe mineralization. Additionally, the occurrence of andradite-rich garnet in skarn and magnetite with high $\delta^{18}O$ values reveals that the magnetite crystallized from the ore-forming fluids has high oxygen fugacity, which is another important factor controlling the occurrences of numerous iron deposits in the Handan–Xingtai iron district.

Conclusion

1. Based on the field investigation and the SHRIMP zircon U–Pb dating, we conclude that magma emplacement and mineralization in the Pingshun deposit took place at 125–123 Ma.
2. Data from S, H–O isotopic compositions and microthermometry of fluid inclusions indicate that the ore-forming fluids were originated from magmas mixed with additional meteoric water and crustal materials with high $\delta^{18}O$ values.
3. It can be inferred that the pre-ore–forming fluid evolved from high temperature and high salinity with enriched Cl and Fe in the pre-ore stage to post-ore stage with moderate to low temperature and salinity. This suggests that the precipitation of magnetite was caused by the significant change of fluid temperature and composition due to extensive boiling including secondary boiling with reduced pressure.
4. The metallogenesis in the Handan–Xingtai iron district is a robust example of the geodynamic response to lithosphere thinning in the NCC. The more mantle materials involved in magmas and high oxygen fugacity are considered to be key factors controlling the occurrence of numerous iron deposits in the Handan–Xingtai iron district.

Acknowledgments We thank K.Y Bai and Y.R Liu for assistance during an investigation by the electron microprobe and fluid inclusions microthermometry at Chang'an University, Xi'an, Beijing. Constructive reviews by Prof. J.J Zhu and J.L Feng are appreciated. Two anonymous reviewers and the editor are thanked for proving constructive comments leading to the improvement of the manuscript.

Funding This work was supported by the Nature Science Foundation of China (41402042, 41002064), Fundamental Research Funds for the Central Universities (310827172006; 300102278402), and Geological investigation work project of China Geological Survey (12120115069701). The first author also thanks the China Scholarship Council (CSC) for the financial support during his study in Canada.

Compliance with ethical standards

Conflict of interest The authors declare that they have no conflict of interest.

References

Black LP, Kamo SL, Allen CM, Aleinikoff JN, Davis DW, Korsch RJ, Foudoulis C (2003) TEMORA 1: a new zircon standard for Phanerozoic U-Pb geochronology. Chem Geol 200:155–170

Bodnar RJ (1993) Revised equation and table for determining the freezing point depression of H_2O-NaCl solutions. Geochim Cosmochim Acta 57:683–684

Chen B, Jahn BM, Arakawa Y, Zhai MG (2004) Petrogenesis of the Mesozoic intrusive complexes from the southern Taihang Orogen, North China Craton: elemental and Sr-Nd-Pb isotopic constraints. Contrib Mineral Petrol 148:489–501

Chen B, Tian W, Jahn BM, Chen ZC (2008) Zircon SHRIMP U-Pb ages and in-situ Hf isotopic analysis for the Mesozoic intrusions in south Taihang,

North China Craton: evidence for hybridization between mantle-derived magmas and crustal components. Lithos 102:118–137

Chen Y, Zhang Z, Zhu J (2014) Geochronology of the Anlin iron skarn deposit, Henan Province and insight into the sources of iron. Acta Petrol Sin 30:1307–1321 (in Chinese with English abstract)

Chen FC, Deng J, Shu QH, Li GJ, Cui XL, Zhao F, Wang QF (2016) Geology, fluid inclusions and stable isotopes (O, S) of the Hetaoping distal skarn Zn-Pb deposit, northern Baoshan block, SW China. Ore Geol Rev 90:913–927. https://doi.org/10.1016/j.oregeorev.2016.10.013

Cline JS (2003) How to concentrate copper. Science 302:2075–2076

Compston W, Williams IS, Mayer C (1984) U-Pb geochronology of zircons from Lunar Breccia 73217 using a sensitive high mass-resolution ion microprobe. J Geophys Res 89:525–535

De Hoog JCM, Taylor BE, Van Bergen MJ (2001) Sulphur isotope systematics of basaltic lavas from Indonesia: implications for the sulphur cycle in subduction zones. Earth Planet Sci Lett 189:237–252

Friedman I, O'Neil JR (1977) Data of geochemistry: compilation of stable isotope fractionation factors of geochemical interest, vol 440. US Government Printing Office

Goldstein RH, Reynolds TJ (1994) Systematic of fluid inclusions in diagenetic materials. Soc Sediment Geol Short Course 31:199

Hart SR (1984) A large-scale isotope anomaly in the Southern Hemisphere mantle. Nature 309(5971):753–757

Hawkins T, Smith MP, Herrington RJ, Maslennikov V, Boyce AJ, Jeffries T, Creaser RA (2017) The geology and genesis of the iron skarns of the Turgai belt, northwestern Kazakhstan. Ore Geol Rev 85:216–246

Heinrich CA (2007) Fluid-fluid interactions in magmatic-hydrothermal ore formation. Rev Mineral Geochem 65:363–387

Hoefs J (2009) Stable isotope geochemistry, 6th edn. Springer, Berlin, p 285

Jamtveit B, Wogelius RA, Fraser DG (1993) Zonation patterns of skarn garnets: records of hydrothermal system evolution. Geology 21: 113–116

Jin ZJ, Zhang ZC, Hou T, Santosh M, Han L (2015) Genetic relationship of high-Mg dioritic pluton to iron mineralization: a case study from the Jinling skarn-type iron deposit in the North China Craton. J Asian Earth Sci 1:957–979

Kesler SE (2005) Ore-forming fluids. Elements 1(1):13–18

Lee J, Williams I, Ellis D (1997) Pb, U and Th diffusion in nature zircon. Nature 390(13):159–162

Li SR, Santosh M (2014) Metallogeny and craton destruction: records from the North China Craton. Ore Geol Rev 56:376–414

Li N, Feng ZY, Yu F (1989) Genesis of the Beiluoxia skarn iron deposit in Shanxi Province: fluid inclusion evidence. Mineral Deposits 8:43–54

Li SR, Santosh M, Zhang HF, Shen JF, Dong GC, Wang JZ, Zhang JQ (2013) Inhomogeneous lithospheric thinning in the central North China Craton: zircon U-Pb and S-He-Ar isotopic record from magmatism and metallogeny in the Taihang Mountains. Gondwana Res 23(1):141–160

Ludwig KR (2001a) Squid 1.02. A user manual. Berkeley Geochronological Center Special, Berkeley, pp 1–219

Ludwig KR (2001b) Using Isoplot/EX, version 2.49. A geochronological toolkit for Microsoft Excel. Berkeley Geochronological Center Special Publication, Berkeley, pp 1–55

Luo G, Zhang ZY, Du YS, Pang ZS, Zhang YW, Jiang YW (2015) Origin and evolution of ore-forming fluids in the Hemushan magnetite-apatite deposit, Anhui Province, eastern China, and their metallogenic significance. J Asian Earth Sci 113:1100–1116

Mei W, Lü XB, Cao XF, Liu Z, Zhao Y, Ai ZL, Tang RK, Abfaua MM (2015) Ore genesis and hydrothermal evolution of the Huanggang skarn iron–tin polymetallic deposit, southern Great Xing'an ng'an range: evidence from fluid inclusions and isotope analyses. Ore Geol Rev 64:239–252

Meinert LD, Dipple GM, Nicolescu S (2005) World skarn deposits. Econ Geol 100:299–336

Mollai H, Sharma R, Pe-Piper G (2009) Copper mineralization around the Ahar batholith, north of Ahar (NW Iran): evidence for fluid evolution and the origin of the skarn ore deposit. Ore Geol Rev 35:401–414

Palinkaš SS, Palinkaš LA, Renac C, Spangenberg JE, Lűders V, Molnar F, Maliqi G (2013) Metallogenic model of the Trepča Pb-Zn-Ag deposit, Kosovo: evidence from fluid inclusions, rare earth elements, and stable isotope data. Econ Geol 108:135–162

Peng TP, Wang YJ, Fan WM (2004) SHRIMP zircon U-Pb geochronology of the diorites for southern Taihang Mountains in the North China interior and its petrogenesis. Acta Petrol Sin 20:253–1262 (in Chinese with English abstract)

Peng HJ, Mao JW, Hou L, Shu QH, Zhang CQ, Liu H, Zhou YM (2016) Stable isotope and fluid inclusion constraints on the source and evolution of ore fluids in the Hongniu-Hongshan Cu skarn deposit, Yunnan province, China. Econ Geol 11:1369–1396

Qian Q, Hermann J (2010) Formation of high-Mg diorites through assimilation of peridotite by monzodiorite magma at crustal depths. J Petrol 51:1381–1416

Qu XM, Hou ZQ, Zaw K, Li YG (2007) Characteristics and genesis of Gangdese porphyry copper deposits in the southern Tibetan Plateau: preliminary geochemical and geochronological results. Ore Geol Rev 31:205–223

Seltmann R, Porter TM (2005) The porphyry Cu-Au/Mo deposits of Central Eurasia: 1. Tectonic, geologic and metallogenic setting and significant deposits. In: Porter TM (ed) Super porphyry copper and gold deposits: a global perspective, vol 2. PGC Publishing, Adelaide, pp 467–512

Seltmann R, Porter TM, Pirajno F (2014) Geodynamics and metallogeny of the central Eurasian porphyry and related epithermal mineral systems: a review. J Asian Earth Sci 79:810–841

Shen BF, Lu SN, Yu NZ, Shan LF, Yu JH (1977) The characteristics of sodium metasomatism in magnetite deposits of a certain region and its prospecting significance. Sci Geol Sin 3:263–274 (in Chinese with English abstract)

Shen P, Shen YC, Li XH, Pan HD, Zhu HP, Meng L, Dai HW (2012) Northwestern Junggar Basin, Xiemisitai Mountains, China: a geochemical and geochronological approach. Lithos 140-141:103–118

Shen JF, Li SR, Santosh M, Meng K, Dong GC, Wang YJ, Yin N, Ma GG, Yu HJ (2013a) He-Ar isotope geochemistry of iron and gold deposits reveals heterogeneous lithospheric destruction in the North China Craton. J Asian Earth Sci 78:237–247

Shen JF, Santosh M, Li RS, Zhang HF, Yin N, Dong GC, Wang YJ, Ma GG, Yu HJ (2013b) The Beiminghe skarn iron deposit, eastern China: geochronology, isotope geochemistry and implications for the destruction of the North China Craton. Lithos 156-159:218–229

Shen JF, Li RS, Santosh M, Dong GC, Wang YJ, Liu HM, Peng ZD, Zhang HF (2015) Zircon U-Pb geochronology of the basement rocks and dioritic intrusion associated with the Fushan skarn iron deposit, southern Taihang Mountains, China. J Asian Earth Sci 113: 1132–1142

Shi ZL, Xiong PF, Wang DY, Jin ZM, Zhang ZG, Huang KK, Feng ZL (1983) Some genesis problems about the Daye type iron deposits of Tieshan from Hubei province. Geol Sci Technol Inf 1:10–29 (in Chinese with English abstract)

Sterner SM, Hall DL, Bodnar RJ (1988) Synthetic fluid inclusions. V. Solubility relations in the system NaCl-KCl-H_2O under vapor-saturated conditions. Geochim Cosmochim Acta 52:989–1005

Sun, SS, McDonough, WF (1989) Chemical and isotopic systematics of oceanic basalts: implications for mantle composition and processes. Geological Society, London, Special Publications, 42(1): 313–345

Sun Y, Xiao L, Zhu D, Wu T, Deng X, Bai M, Wen G (2014) Geochemical, geochronological, and Sr-Nd-Hf isotopic constraints on the petrogenesis of the Qicun intrusive complex from the Handan-Xingtai district: implications for the mechanism of lithospheric thinning of the North China Craton. Ore Geol Rev 57: 363–374

Taylor HP (1974) The application of oxygen and hydrogen isotope studies to problems of hydrothermal alteration and ore deposition. Econ Geol 69:843–883

Taylor BE (1976) Origin and significance of C-O-H fluids in the formation of Ca-Fe-Si skarn, Osgood Mountains, Humboldt County, Nevada. Ph.D. thesis. Stanford University, p 306

Taylor HP Jr (1997) Oxygen and hydrogen isotope relationships in hydrothermal deposits. In: Barnes HL (ed) Geochemistry of hydrothermal deposits, 3rd edn. Wiley, New York, pp 229–302

Taylor SR, McLennan SM (1985) The continental crust: its composition and evolution. Blackwell Scientific, Oxford

Vallance J, Fontboté L, Chiaradia M, Markowski A, Schmidt S, Vennemann T (2009) Magmatic-dominated fluid evolution in the Jurassic Nambija gold skarn deposits (southeastern Ecuador). Mineral Deposita 44:389–413

Wang YJ, Fan WM, Zhang HF, Peng TP (2006) Early Cretaceous gabbroic rocks from the Taihang Mountains: implication for a paleosubduction-related lithospheric mantle beneath the central North China Craton. Lithos 86:281–302

Wilde SA, Zhao G, Sun M (2002) Development of the North China Craton during the late Archaean and its final amalgamation at 1.8 Ga: some speculations on its position within a global Palaeoproterozoic supercontinent. Gondwana Res 5:85–94

Wilkinson JJ (2001) Fluid inclusions in hydrothermal ore deposits. Lithos 55:229–272

Williams IS, Claesson S (1987) Isotope evidence for the Precambrian provenance and Caledonian metamorphism of high grade paragneisses from the Seve Nappes, Scandinavian Caledonides. Ion microprobe zircon U-Th-Pb. Contrib Mineral Petrol 97:205–217

Wu FY, Xu YG, Gao S, Zheng JP (2008) Lithospheric thinning and destruction of the North China Craton. Acta Petrol Sin 24:1145–1174 (In Chinese with English abstract)

Xu WL, Yang DB, Pei RF, Yu Y (2009) Petrogenesis of Fushan high-$Mg^{\#}$ diorite from the northern Taihang Mts. in the central North China Craton: resulting from interaction of peridotite-melt derived from partial melting of delaminated lower continental crust. Acta Petrol Sin 25:1947–1961 (in Chinese with English abstract)

Xu LG, Mao JW, Yang FQ, Daniel H, Zheng JM (2010a) Geology, geochemistry and age constraints on the Mengku skarn iron deposit in Xinjiang Altai, NW China. J Asian Earth Sci 39:432–440

Xu WL, Wang CG, Yang DB, Wang F, Pei FP (2010b) Dunite xenoliths and olivine xenocrysts in gabbro from Taihang Mountains: characteristics of Mesozoic lithospheric mantle in central China. J Earth Sci China 21:692–170

Xu WL, Yang DB, Gao S, Pei FP, Yu Y (2010c) Geochemistry of peridotite xenoliths in early cretaceous high-$Mg^{\#}$ diorites from the central orogenic block of the North China Craton: the nature of Mesozoic lithospheric mantle and constraints on lithospheric thinning. Chem Geol 270:257–273

Yang JH, Wu FY, Wilde SA, Belousova E, Griffin WL (2008) Mesozoic decratonization of the North China block. Geology 36:467–470

Yardley BWD, Rochelle CA, Barnicoat AC, Lloyd GE (1991) Oscillatory zoning in metamorphic minerals: an indicator of infiltration metasomatism. Mineral Mag 55:357–365

Zartman RE, Doe BR (1981) Plumbotectonics—the model. Tectonophysics 75:135–162

Zhai MG, Santosh M (2011) The early Precambrian odyssey of the North China Craton: a synoptic overview. Gondwana Res 20:6–25

Zhang HD, Liu JC, Chen ZL, Liu SW, Ge XH, Cheng H, Zhang X (2010) Geological characteristics of skarn iron deposits and their mineralization material sources in the Pingshun area, Shanxi Province. Geol Explor 46:634–642 (in Chinese with English abstract)

Zhang HD, Liu JC, Peng SX, Zhang SN, Men WH, Wang RM, Wu JL, Huang SW (2013) Ore-forming material sources of the Pingshun iron deposits in the southern Taihang Mountains: constraints from trace elements and S and Pb isotopes. Geol Explor 249:1088–1097 (in Chinese with English abstract)

Zhang HD, Liu JC, Chen ZL, Chen BL, Peng SX, Men WH (2014) Petrogensis of the Pingshun complexes in the southern Taihang Mountains: petrology, geochronology and geochemistry. Geotecton Metallog 38:454–471

Zhang HD, Liu JC, Santosh M, Tao N, Zhou QJ, Hu B (2017) Ultra-depleted peridotite xenoliths in the northern Taihang Mountains: implications for the nature of the lithospheric mantle beneath the North China Craton. Gondwana Res 48:72–85

Zhao YM, Lin WW, Bi CS, Li DX, Jiang CJ (1990) Skarn deposit of China. Geological Publishing House, pp 1–354 (in Chinese)

Zhao G, Wilde SA, Cawood PA, Sun M (2001) Archean blocks and their boundaries in the North China Craton: lithological, geochemical, structural and P-T path constraints and tectonic evolution. Precambrian Res 107:45–73

Zheng JM (2007) The ore-forming fluid and mineralization of skarn Fe deposits in Handan-Xingtai Area, South Hebei (Ph.D. thesis). The China University of Geosciences, 1-107 (in Chinese with English abstract)

Zheng YF, Chen JF (2000) Stable isotope geochemistry, vol 10. Sci. Press, Beijing, p 12

Zheng YF, Hoefs J (1993) Carbon and oxygen isotopic covariations in hydrothermal calcites. Mineral Deposita 28(2):79–89

Zheng YF, Satir M, Metz P (1995) Oxygen isotope fractionation in amphiboles. Sci Geol Sin 30:1–11 (in Chinese with English abstract)

Zheng J, Chen M, Xu L, Gao J, Hu Y, Liang Z (2006) Characteristics of structurally controlled skarn iron deposits and prospecting targets in Handan-Xingtai area. Mineral Deposits 25:115–118 (in Chinese with English abstract)

Zheng JM, Mao JW, Chen M, Li G, Ban C (2007a) Geological characteristics and metallogenic model of skarn iron deposits in the Handan-Xingtai area, Southern Hebei, China. Geol Bull China 26:150–154 (in Chinese with English abstract)

Zheng JM, Xie GQ, Liu J, Chen HM, Wang SM, Guo SF, Gao X, Li GD (2007b) ^{40}Ar-^{39}Ar dating of phlogopite from the Xishimen skarn iron deposit in the Handan-Xingtai area, southern Hebei, and its implications. Acta Petrol Sin 23:2513–2518 (in Chinese with English abstract)

Zhou ZH, Mao JW, Che HW, Ouyang HG, Ma XH (2017) Metallogeny of the Handagai skarn Fe–Cu deposit, northern Great Xing'an range, NE China: constraints on fluid inclusions and skarn genesis. Ore Geol Rev 80:623–644

Zhu R, Chen L, Wu F, Liu J (2011) Timing, scale and mechanism of the destruction of the North China Craton. Sci China Earth Sci 54(6):789–797

Zhu QQ, Li W, Zhang ZY, Han YX, Wang J (2016) Tracing incursion of the evaporites into Jinshandian skarn Fe deposit, Hubei province, by combination of multiple stable isotopes. Acta Geol Sin 90:361–375 (in Chinese with English abstract)

Zong X, Jia D, Liu C, Yin C, Liu J, Wang J (2010) Study on ore occurrence of Laiwu contact and geothermal metasomatic iron deposit in Shandong province. Land Resour 26:13–18 (in Chinese with English abstract)